International Journal of Nanomedicine Dovepress

Open Access Full Text Article ORIGINAL RESEARCH

RNA-Seq Reveals the Mechanism of Pyroptosis Induced by Oxygen-Enriched IR780 Nanobubbles-Mediated Sono-Photodynamic Therapy

Xiang He[1,*], Yuhang Tian[1,*], Jialin Dong[1], Yanchi Yuan[1], Shijie Zhang[2], Hui Jing[1]

[1]Department of Ultrasound, Harbin Medical University Cancer Hospital, Harbin, People's Republic of China; [2]Department of Radiation Oncology, Harbin Medical University Cancer Hospital, Harbin, People's Republic of China

*These authors contributed equally to this work

Correspondence: Hui Jing, Department of Ultrasound, Harbin Medical University Cancer Hospital, No. 150, Haping Road, Nangang District, Harbin, 150081, People's Republic of China, Email jinghuihrb@163.com

Background: Sono-photodynamic therapy (SPDT), the combination of sonodynamic therapy (SDT) and photodynamic therapy (PDT), is a promising tumor treatment method. However, the hypoxic tumor microenvironment greatly compromises the efficacy of SPDT. Pyroptosis, a new type of programmed cell death, is mainly induced by some chemotherapeutic drugs in the current research, and rarely by SPDT. RNA sequencing (RNA-seq) is a high-throughput sequencing technique that comprehensively profiles the transcriptome, revealing the full spectrum of RNA molecules in a cell. Here, we constructed IR780@O_2 nanobubbles (NBs) with photoacoustic dual response and hypoxia improvement properties to fight triple negative breast cancer (TNBC), and demonstrated that SPDT could kill TNBC cells through pyroptosis pathway. RNA-seq further revealed potential mechanisms and related differentially expressed genes.

Methods: Thin-film hydration and mechanical vibration method were utilized to synthesize IR780@O_2 NBs. Subsequently, we characterized IR780@O_2 NBs and examined the cytotoxicity as well as ROS production ability. A series of experiments were conducted to verify that SPDT killed TNBC cells through pyroptosis.

Results: IR780@O_2 NBs were successfully prepared and had certain stability. Compared with SDT alone, SPDT increased therapeutic effect by 1.67 times by generating more ROS, and the introduction of NBs and O_2 NBs (2.23 times and 2.93 times compared with SDT alone) could further promote this process. Other experiments proved that TNBC cells died by pyroptosis pathway. Moreover, the in-depth mechanism revealed that colony stimulating factor (CSF) and C-X-C motif chemokine ligand (CXCL) could be potential targets for the occurrence of pyroptosis in TNBC cells.

Conclusion: The IR780@O_2 NBs prepared in this study increased the degree of TNBC cell pyroptosis through SPDT effect and alleviation of hypoxia, and cellular senescence might be a biological process closely related to pyroptosis in TNBC.

Keywords: triple negative breast cancer, sono-photodynamic therapy, hypoxia relief, pyroptosis, RNA-seq

Introduction

Breast cancer (BC) has seriously endangered women's health. Triple negative breast cancer (TNBC), a special subtype of BC, is characterized by the lack of expression of estrogen receptor (ER), progesterone receptor (PR) as well as human epidermal growth factor receptor-2 (HER2).[1] Compared with other subtypes of BC, TNBC is more aggressive with a higher recurrence rate and mortality, and its treatment methods are limited and the curative effect is poor due to the lack expression of receptors.[2] Even as the most commonly used therapeutic modality for TNBC in clinical practice, chemotherapy still cannot effectively improve the prognosis of patients.[2] Hence, the pursuit of an innovative and

Received: 2 September 2024
Accepted: 23 November 2024
Published: 4 December 2024

efficacious therapeutic approach for TNBC holds considerable importance. Fortunately, the era of nanomedicine for combating tumors has flourished, largely due to the swift advancement in nanotechnological innovations.[3–5]

Photodynamic therapy (PDT), as a typical representative of nanomedicine, is a non-invasive, effective, and spatiotemporal controllable anti-tumor method, which makes use of photosensitizers (PSs) to generate reactive oxygen species (ROS) under light irradiation to kill tumor cells.[6] However, the constrained capacity for light to penetrate significantly undermines the effectiveness of PDT, preventing the complete eradication of deep tumors and hindering the clinical transformation of PDT.[7] Alternately, sonodynamic therapy (SDT), another promising nanotherapy that overcomes tumors through the ROS generated by sonosensitizers under low-intensity ultrasound (US) irradiation, has excellent curative effect in deep tumors owing to the better penetration characteristics of US.[8] Nevertheless, the relatively low generation of ROS during SDT may require a larger dose of sonosensitizers, which will undoubtedly lead to greater side effects.[9] It has been widely recognized that the anti-tumor effect of sono-photodynamic therapy (SPDT) which combines SDT and PDT is superior to that of SDT or PDT alone, as the simultaneous application of light and US will increase the generation of ROS.[10–12] Moreover, numerous sensitizers such as indocyanine green, IR780, and curcumin can not only produce PDT effect under light irradiation but also SDT effect under US irradiation, so as to reduce the dosage of sensitizers and increase biocompatibility through this dual-use way of single material.[13–15]

Although SPDT has better tumor treatment efficacy than SDT and PDT alone, it still has some limitations. Whether SDT, PDT, or SPDT, oxygen is required as a reactant to produce ROS, which is extremely compromised by the hypoxic tumor microenvironment (TME).[16] Fortunately, researchers have found that nanobubbles (NBs) with gas core have enormous potential in alleviating tumor hypoxia and drug delivery.[17,18] On the one hand, the gas core of NBs can be filled with oxygen to improve tumor hypoxia and increase the efficacy of SPDT. On the other hand, the unique biological effects produced by NBs under US irradiation, namely ultrasound targeted nanobubble destruction (UTND) technology, can increase the local drug concentration in tumors.

Pyroptosis, a new mode of programmed cell death, is characterized by the rupture of cell membrane and the release of cytoplasmic contents.[19] During the process of pyroptosis, gasdermin (GSDM) family proteins are cleaved by activated caspases to release effector domain (GSDM-N), which can bind to the cell membrane and form pores on it.[19–21] Generally, current studies have shown that pyroptosis is mainly induced by several chemotherapeutic drugs through two pathways, including caspase-1/GSDMD-N and caspase-3/GSDME-N, while the latter plays a dominant role in TNBC.[22,23] However, chemotherapy has great side effects. Although it can effectively induce tumor cell pyroptosis, the non-specific distribution of drugs seriously damages normal tissues. Since chemotherapy can activate caspase to induce pyroptosis through the production of ROS, and there are currently few experimental studies on SPDT induced TNBC cell pyroptosis, which makes it valuable to verify that SPDT can induce TNBC cell death through the pyroptosis pathway.[22,23]

RNA sequencing (RNA-seq) is a high-throughput sequencing technique that comprehensively profiles the transcriptome, revealing the full spectrum of RNA molecules in a cell.[24,25] It enables differential gene expression analysis, uncovering the molecular mechanisms underlying biological processes and diseases.[26] This powerful tool has facilitated the study of transcriptional dynamics, alternative splicing, and non-coding RNAs, advancing our understanding of gene regulation and function.

In this manuscript, we construct multifunctional NBs with photoacoustic dual responsiveness and tumor hypoxia improvement properties. The synthesized IR780@O_2 NBs can exert SPDT effect under the sequential irradiation of US and near-infrared light (NIR), and the destruction of NBs release oxygen to improve the hypoxic TME and produce UTND effect to promote the entry of IR780 into tumor cells. Since ROS is a driving agent of pyroptosis, we explore whether SPDT is an effective way to induce pyroptosis in TNBC cells, and whether IR780@O_2 NBs can promote tumor enrichment of drugs and improve the hypoxic microenvironment, exacerbating the degree of pyroptosis. At last, RNA-seq further reveals potential mechanisms and related differentially expressed genes (Figure 1).

Materials and Methods

Preparation of IR780 NBs, O_2 NBs, and IR780@O_2 NBs

The details of reagents, cell line and apparatus are in the Chemicals and Apparatus section of the supporting information. IR780, along with 1.2-Distearoyl-sn-glycero-3-phosphocholine (DSPC), and 1.2-distearoyl-sn-glycero-3-phosphoethanolamine-N

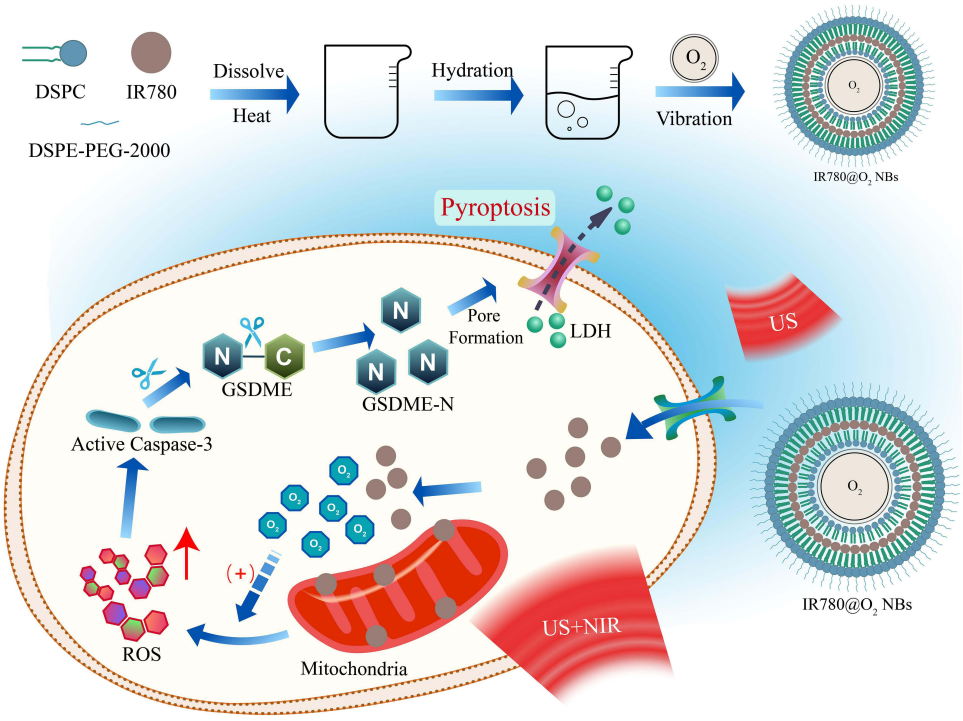

Figure 1 Schematic illustration of IR780@O_2 NBs-induced pyroptosis through SPDT in MDA-MB-231 cells.

(methoxy[polyethylene glycol]-2000) (DSPE-PEG-2000) were combined in a weight ratio of 1:18:2, respectively. This mixture was then dissolved in a solution of methanol and methylene chloride, mixed in a 1:2 volume ratio. The resulting homogeneous suspension was subsequently conveyed to a water bath set at 60 °C for evaporation, aiming to form a lipid film. The lipid film was rehydrated using pre-warmed phosphate-buffered saline (PBS), yielding a lipid suspension, which was then repeatedly extruded 40 times through a 400 nm membrane with a small extrude. The uniform lipid suspension was filled in an airtight vial with a three-way tube, drained the gas in the vial, and rotated the three-way tube to inject pure oxygen. Subsequently, the vial was shaken intensely for 60 seconds using a dental vibrator to form the end product. Then, the synthesized IR780@O_2 NBs was purified by centrifuging to remove the unloaded drugs and other excess materials and finally resuspended in an appropriate amount of PBS. Similarly, IR780 NBs and O_2 NBs were produced in the same process, while the air in IR780 NBs was replaced by perfluoropropane. All compounds were stored at 4 °C.

Characterization

The morphology of IR780@O_2 NBs were examined using a transmission electron microscope (TEM). The dynamic light scattering (DLS) technique was employed to determine the zeta potential and the dimensions of the particles. The absorption spectrums of the particles were detected by an ultraviolet-visible spectrophotometer. Moreover, in order to evaluate the stability of IR780@O_2 NBs, the particle size after 15 d of preparation was measured. The encapsulation and loading efficiency of IR780 were calculated by a standard curve. The encapsulation efficiency of IR780 was obtained by dividing weight of loaded IR780 entrapped inside the NBs by weight of initially added IR780 and multiplying 100%, while the loading efficiency of IR780 was obtained by dividing weight of loaded IR780 entrapped inside the NBs by the weight of lipid used to prepare the NBs and multiplying 100%.

In vitro Release Kinetics

IR780 and O_2 responsive release from IR780@O_2 NBs were tested under different pHs (6.8 and 7.4) with or without US. As for the release of IR780, IR780@O_2 NBs solution (1 mL, 1 mg/mL IR780) was introduced into a dialysis bag with a molecular weight limit of 2000 Da, and this bag was immersed in 10 mL of the appropriate buffer solution.

Subsequently, at each predetermined time point, 1 mL of the external phase buffer solution was extracted and analyzed using an ultraviolet-visible spectrophotometer, while an equivalent volume of the corresponding buffer solution was replenished to the outer phase. Regarding the release of O_2, IR780@O_2 NBs solution was immersed in a closed vial containing hypoxic solution, and the O_2 concentration in the solution at different time points was measured with an oximeter.

Cell Culture and Treatment

The MDA-MB-231 cells were cultured in Leibovitz's L15 medium containing 10% fetal bovine serum (FBS) and 1% penicillin-streptomycin in a sterile incubator without CO_2 at 37 °C.

As for treatment, there were five groups in this study: the control group (Control), IR780 plus US group (SDT), IR780 plus US and NIR group (SPDT), IR780 NBs plus US and NIR group (SPDT NBs), and IR780@O_2 NBs plus US and NIR group (SPDT + O_2 NBs). The US and NIR parameters were as follows: US: frequency: 1 MHz, power density: 3.5 W/cm^2, duty cycle: 50%, irradiation time: 90s; NIR: wavelength: 808 nm, power density: 1 W/cm^2, irradiation time: 30s.

Cell Viability Assay

In order to evaluate the toxicity of synthesized IR780@O_2 NBs, MDA-MB-231 cells were seeded onto 96-well plate at 1.5×10^4 per well. After cell adhesion, fresh L15 medium, with varying concentrations of IR780@O_2 NBs (0, 1, 2.5, 5, 7.5, 10 μg/mL IR780), was substituted for the existing culture medium. After 24 h, L15 was discarded and a mixture of 100 μL serum free culture medium and CCK-8 was added at a volume ratio of 9:1. Following 1 h of incubation in the dark at a temperature of 37 °C, a microplate reader was utilized to determine the optical density (OD) at 450 nm for each well. Similarly, the same process was used to detect cell viability in different groups after 24 h of treatment, and the IR780 concentration of IR780@O_2 NBs in the grouping experiment was 1 μg/mL.

Staining of Live/Dead Cells

24-well plate was utilized for the cultivation of cells, with a seeding density of 1.5×10^5 cells per well. After 24 h of treatment, the cells underwent rinsing with PBS. Subsequently, 500 μL of Calcein-AM/PI solution, prepared at an appropriate dilution, was introduced to the wells. The cells were then subjected to a 30-minute incubation at a temperature of 37 °C in a dark environment. The last step involved the examination of the cells using a fluorescence microscope.

Detection of ROS

MDA-MB-231 cells were plated in a 24-well format, with each well receiving a density of 1.5×10^5 cells. After 2 h of treatment, the cells were rinsed twice using PBS. Subsequently, 500 μL of an appropriately diluted 2.7-dichlorodihydro-fluorescein diacetate (DCFH–DA) solution was applied to the cells, which were then placed in an incubator set to 37 °C under dark conditions for a duration of 25 minutes. To eliminate any unbound DCFH-DA, the cells were washed thrice with a serum-free culture medium. The cells were then promptly analyzed under fluorescent microscopy.

Microscopic Imaging

In order to observe the changes of cell morphology during pyroptosis, cells after 12 h of treatment were placed under a LEICA Camera microscope for photography and post-processed with Adobe Photoshop.

Mitochondrial Membrane Potential Test

Mitochondrial membrane potential was analyzed by JC-1 kit and observed under a fluorescence microscope. Briefly, after 24 h of treatment, MDA-MB-231 cells were stained by JC-1 kit in the dark for 20 minutes, followed by washing with JC-1 staining buffer twice, and then adding culture medium for observation under a fluorescence microscope.

Flow Cytometry Assay

The double staining of annexin V and PI detected by flow cytometry was used to evaluate the degree of pyroptosis in MDA-MB-231 cells. In accordance with the provided guidelines, the MDA-MB-231 cells post-treatment were gathered and rinsed twice using pre-cooled PBS. Subsequently, the cells underwent staining with annexin V-AbFluor™ 488 and PI, followed by a 15-minute incubation period at room temperature in a dark setting. Following this, annexin V binding buffer was introduced, the mixture was gently mixed, and then it was transferred to an ice bath. The cells were then analyzed using flow cytometry.

Lactate Dehydrogenase (LDH) Release Assay

The release of LDH from treated cell supernatant could be used to evaluate the degree of pyroptosis. According to the instructions, cells were seeded onto 96 well plate at 1.5×10^4 per well. After the cells were treated as before, the supernatant of each well was added to the corresponding well of a new 96 well plate and LDH detection working solution was added, and then incubated at room temperature in the dark for 30 minutes and the OD values were measured at 490 nm. The release data of LDH in each group were presented as a percentage of the total LDH level in supernatant.

Western Blot

Western blot analysis was employed to assess the levels of proteins associated with pyroptosis. Briefly, following the designated treatment protocol, the MDA-MB-231 cells were harvested, subjected to lysis, and proteins were subsequently isolated and quantified. The prepared protein samples were electrophoresed on 12.5% polyacrylamide gel electrophoresis and transferred to nitrocellulose filter membrane, and then blocked with 5% skimmed milk for 1 h at room temperature and incubated with antibodies overnight at 4 °C, including cleaved-caspase-3, cleaved-GSDME (GSDME-N) and GAPDH. After washing three times and incubating the secondary antibody at room temperature for 1 h, the protein bands were observed after washing three more times. The quantification of protein bands intensities was carried out utilizing the Image J software.

Whole Transcriptome Library Construction, Sequencing, and Analysis

The total RNA of MDA-MB-231 cells before and after SPDT + O_2NBs treatment was isolated and tested, respectively, named A and B group, and quality assurance measures were implemented. The comprehensive transcriptome library's assembly and its meticulous sequencing were both conducted by the efforts of Novogene Bioinformatic.

RNA Quantification and Qualification

The overall quantity and completeness of RNA were evaluated through the application of the RNA Nano 6000 Assay Kit of the Bioanalyzer 2100 system.

Library Preparation for Sequencing

Each sample contributed 1 μg of total RNA as the starting material for preparing the library. The creation of strand-specific libraries adhered to the NEBNext®

UltraTM RNA Library Prep Kit for Illumina® protocol, as per the manufacturer's guidance, with unique index codes appended to identify and track the sequences back to their respective samples.

Clustering and Sequencing

Once the library had passed quality assessment, the various libraries were consolidated based on their effective concentrations and the desired data yield from the sequencing instrument, and were subsequently sequenced on the Illumina NovaSeq 6000 platform.

Quality Control

Initially, the raw data in the form of fastq reads were subjected to processing by our proprietary perl scripts. During this phase, the extraction of clean reads from the raw data was achieved by removing reads that included adapters, stretches

of poly-N, or exhibited low quality. Concurrently, the calculation of the Q20, Q30, and GC content for the clean reads was executed. Subsequent analyses were conducted utilizing the high-quality clean data.

Quantification of Gene Expression Level

(Stringtie-1.3.3b) was deployed to tally the quantity of reads aligned to individual genes. Subsequently, the FPKM values were determined, representing the anticipated count of Fragments Per Kilobase of transcript sequence for every Millions of base pairs sequenced. The FPKM method was a straightforward and widely adopted approach for normalizing gene expression levels, considering the sequencing depth and the size of the genome.

Differential Expression Analysis

Before the analysis of differential gene expression, the read counts for each library were modified by applying a uniform scaling normalization factor through the edgeR program suite. The comparative analysis of gene expression between two samples was executed with the edgeR R package version 3.22.5. The P values underwent adjustment according to the method by Benjamini and Hochberg. Genes with significantly different expression were identified using the criterion of a corrected P-value below 0.05.

GO, KEGG, Reactome, and DO Enrichment Analysis of Differentially Expressed Genes

The clusterProfiler R package was utilized to carry out a GO enrichment analysis on the set of differentially expressed genes, with adjustments made for gene length bias. GO terms were deemed significantly enriched if they had a corrected P-value below the threshold of 0.05. Similarly, for the statistical assessment of the enrichment of differentially expressed genes within KEGG, Reactome, and DO pathways, the clusterProfiler R package was again employed.

Statistical Analysis

The experimental results were depicted as mean ± standard deviation and the experiments were repeated at least three times. For statistical processing, GraphPad prism 8 software was selected as the analytical tool. It employed the Student's *t*-test to assess differences in pairs of groups, whereas one-way analysis of variance was applied for evaluating variances among multiple groups, and $P < 0.05$ represented statistical significance.

Results

Characterization of IR780@O_2 NBs

As shown in Figure 2A, the prepared IR780@O_2 NBs exhibited spherical structure under TEM observation. The detection results of DLS indicated that IR780@O_2 NBs had an average size of 395 ± 2.94 nm, slightly larger than the estimated particle size by TEM, which might be caused by partial aggregation of NBs, and the particle size slightly increased with time, which proved a certain stability (Figures 2B and S1). The zeta potential of O_2 NBs was −7.81 ± 0.05 mV, and the potential rose to −4.04 ± 0.42 mV after loading IR780 (Figure 2C). The absorption spectrum in Figure 2D showed that O_2 NBs had no obvious absorption peak, while the synthesized IR780@O_2 NBs had the same peak as IR780, indicating that IR780 was successfully carried on O_2 NBs. To calculate the encapsulation and loading efficiency of IR780, a standard curve was made (Figure S2), in which the encapsulation rate of IR780 was 80.70 ± 3.44%, while the loading rate was 3.84 ± 0.16%. Figure 2E and F indicated that IR780 and O_2 released slowly over time, and the alteration of the pH value did not impact this process. In contrast, following the application of US irradiation, the release of IR780 and O_2 was significantly hastened, demonstrating that IR780@O_2 NBs was an US-responsive nano delivery system.

The Efficacy of SPDT was Superior to SDT Alone and Further Enhanced by NBs and O_2 NBs

Firstly, the cytotoxicity of prepared IR780@O_2 NBs was detected using the CCK-8 assay. As shown in Figure 3A, the cytotoxicity of IR780@O_2 NBs increased with the increase of the concentration of IR780, and there was no obvious

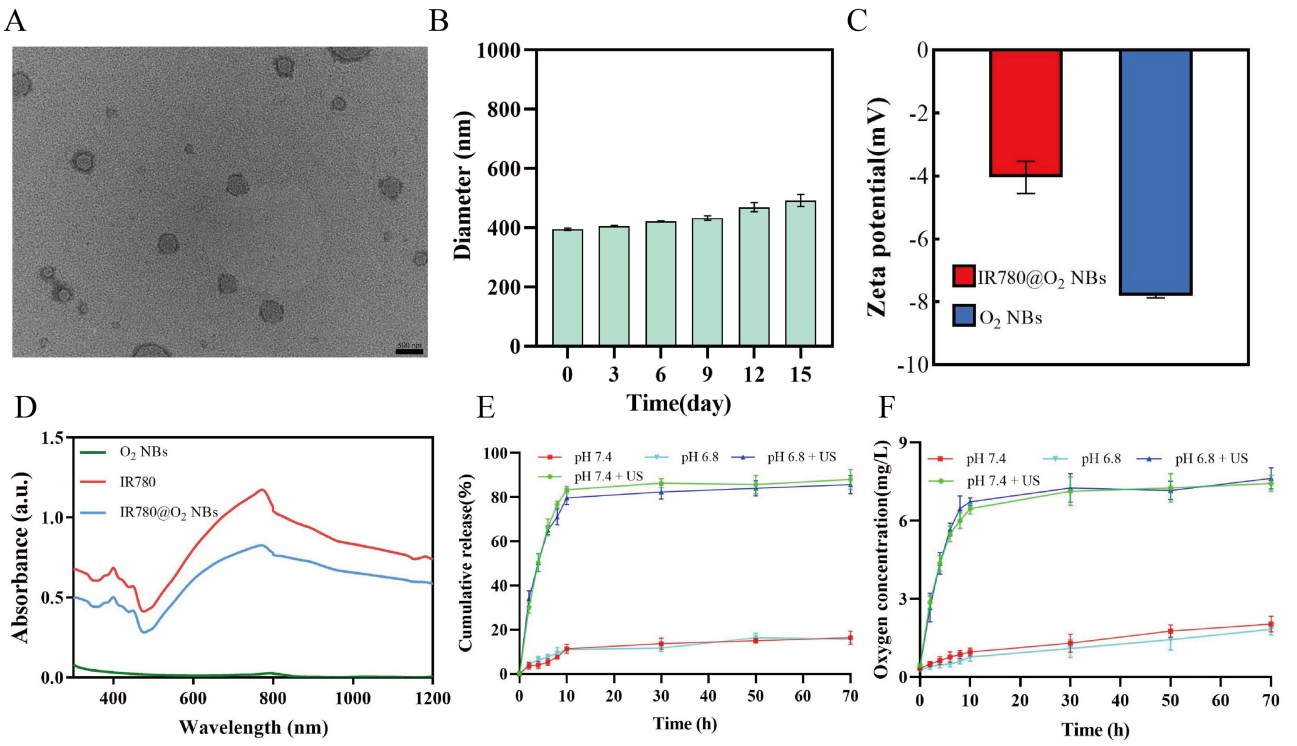

Figure 2 Characterization of the NBs. (**A**) TEM image of IR780@O_2 NBs. (**B**) Size distribution of IR780@O_2 NBs at different times after preparation measured by DLS. (**C**) Zeta potential of O_2 NBs and IR780@O_2 NBs. (**D**) Absorption spectra of IR780, O_2 NBs, and IR780@O_2 NBs. (**E**) and (**F**) The release profiles of IR780 and O_2 at pH 7.4 and 6.8 with or without ultrasound.

cytotoxicity when the concentration was less than 5 μg/mL. As for the grouping experiment, the results in Figure 3B showed that SDT had a certain killing effect on MDA-MB-231 cells, and the cell viability reduced to 77.05 ± 2.98%. The therapeutic efficacy was stronger when combined with PDT (SPDT), with the 61.78 ± 2.84% cell viability. In addition, after the introduction of NBs, the tumor suppressive ability of SPDT was improved (48.78 ± 3.51% cell viability), indicating that NBs could synergize SPDT to kill tumors, and after the addition of oxygen, the tumor cell viability further reduced to 32.74 ± 1.15%, proving that oxygen could synergistically promote the efficacy of SPDT through some mechanisms.

For more intuitive visualization of cell status, Calcein-AM/PI double stain was used to observe the cell survival and death under a fluorescence microscope, in which the dead cells were shown as red fluorescence, while the living cells were shown as green fluorescence. In Figure 3C, significant green fluorescence and less red fluorescence could be seen in the control group, indicating that a large number of cells in the control group survived, but red fluorescence began to appear in the SDT and SPDT groups, indicating that SDT and SPDT killed some MDA-MB-231 cells. When NBs were introduced, more red fluorescence could be observed, and the strongest red fluorescence signal appeared in the SPDT O_2NBs group, indicating that the introduction of oxygen could enhance the killing effect of SPDT on tumor cells. These experimental results were consistent with the results of CCK-8 assay.

Since whether SDT, PDT or SPDT, the principle of tumor killing was through the generation of ROS, we detected the production of ROS in different groups. As shown in Figure 3D, compared with the control group, SDT and SPDT groups had relatively obvious green fluorescence signals (green fluorescence signals represent ROS), and the fluorescence intensity in SPDT NBs group was stronger than that in SDT and SPDT groups. In addition, the introduction of oxygen further enhanced the ROS fluorescence intensity. Consistent with the expectation, the production of ROS was positively correlated with the therapeutic effect. More ROS production would lead to more cell death, and the introduction of oxygen could alleviate tumor hypoxia, increase the production of ROS, and enhance the killing effect of SPDT.

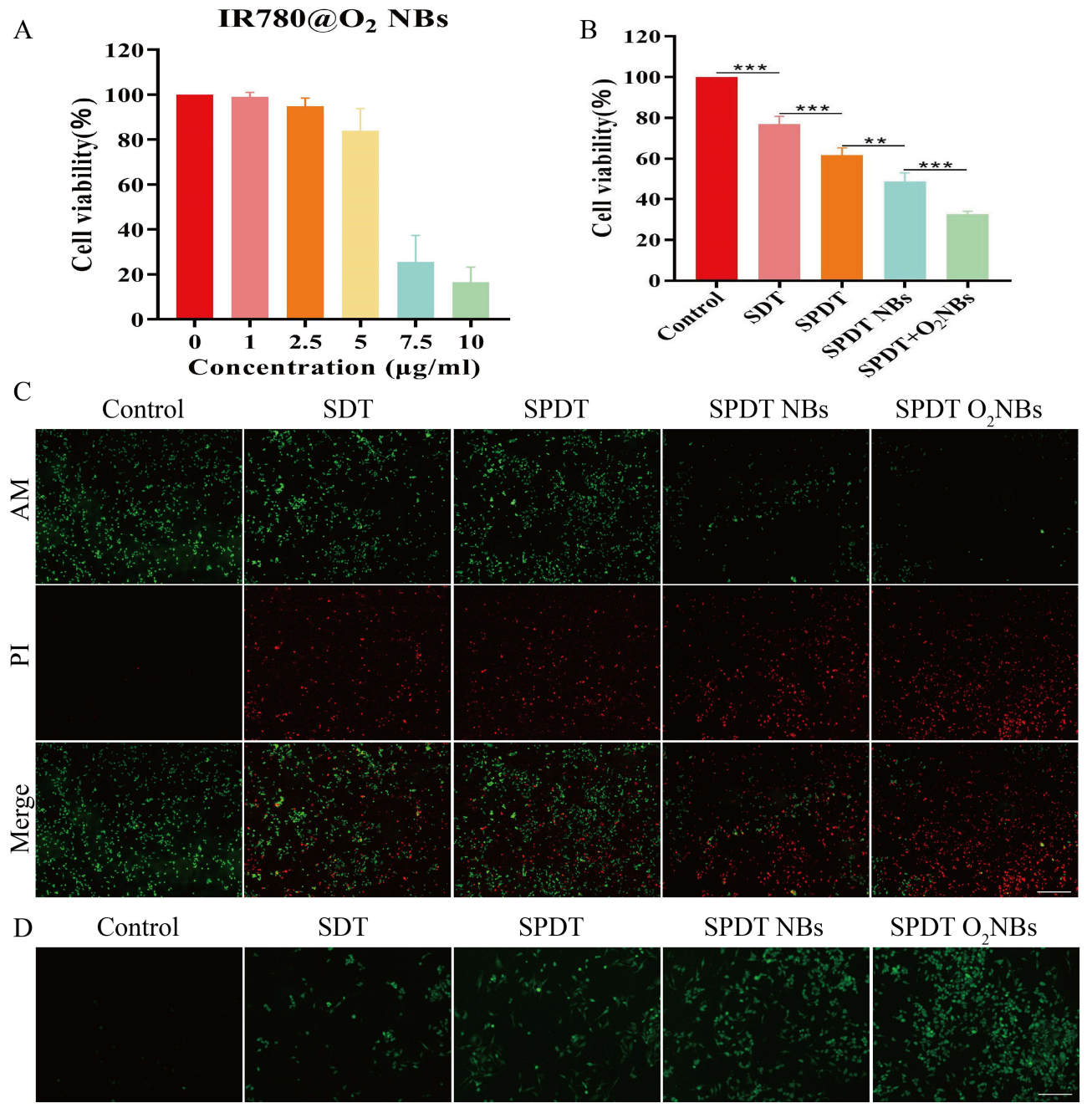

Figure 3 The efficacy of SPDT was superior to SDT alone and further enhanced by NBs and O_2 NBs. (**A**) Cell viability of MDA-MB-231 cells after co-incubation with different concentrations of IR780@O_2 NBs for 24 h. (**B**) Cell viability of MDA-MB-231 cells after different treatments. ***P*<0.01, ****P*<0.001. (**C**) Fluorescence live/dead cell images of MDA-MB-231 cells after different treatments (scale bar:100 μm). (**D**) Fluorescence microscope images of ROS generation after different treatments (scale bar:100 μm).

SPDT Induced Pyroptosis in MDA-MB-231 Cells, and the Introduction of NBs and O_2 NBs Increased the Extent of Pyroptosis

Subsequently, in order to investigate the underlying cell death mechanism, a series of experiments were conducted to verify whether SPDT could kill TNBC cells through pyroptosis pathway. Primarily, the change of cell morphology was the most intuitive manifestation of pyroptosis. The microscopic pictures showed that the cells treated in different groups exhibited varying degrees of peripheral swelling and the formation of large bubbles on the cell membrane, which were not observed in the control group (Figure 4A). Compared with SDT and SPDT groups, SPDT NBs group showed fewer

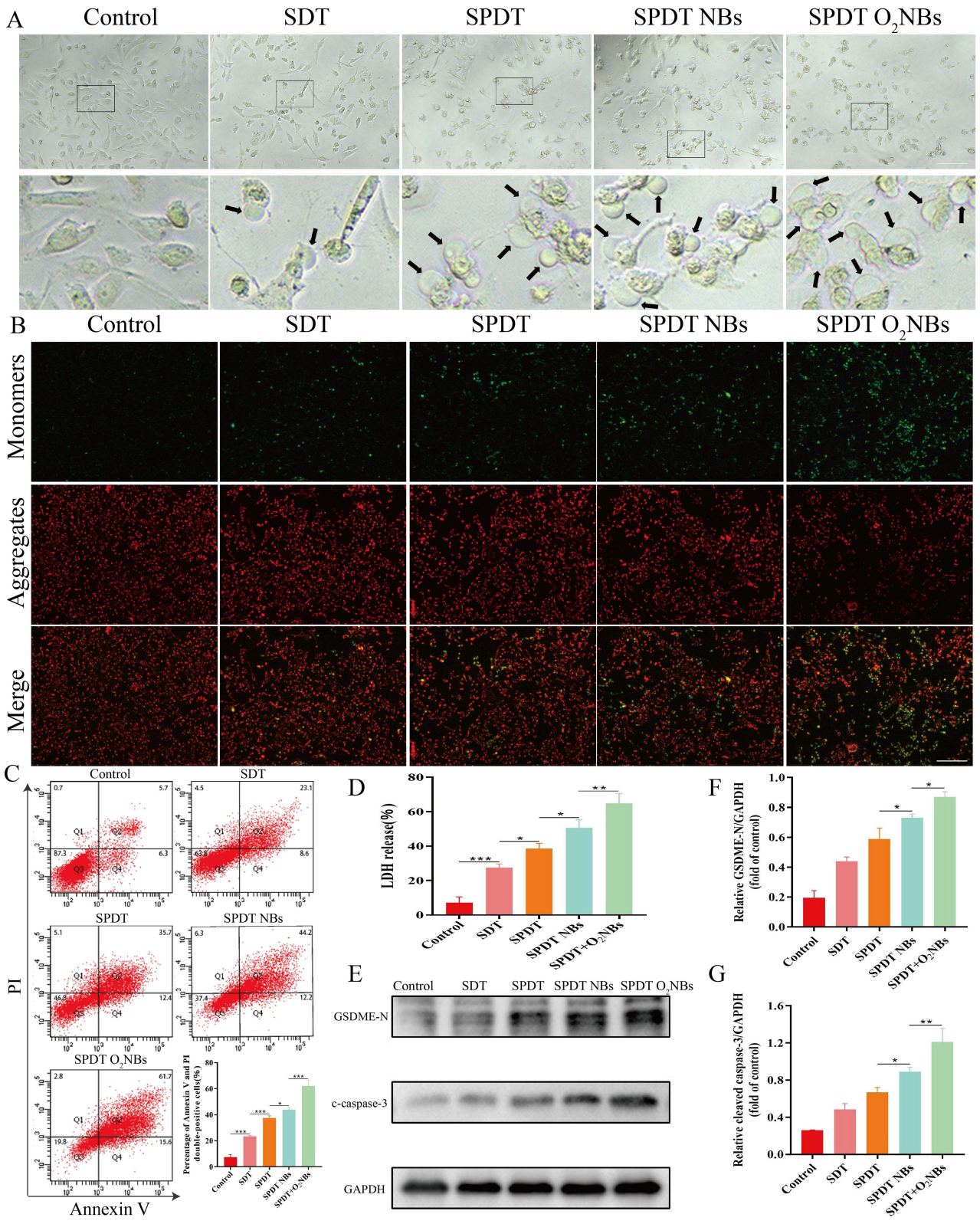

Figure 4 SPDT induced pyroptosis in MDA-MB-231 cells, and the introduction of NBs and O_2 NBs increased the extent of pyroptosis. (**A**) Representative microscope images of MDA-MB-231 cells after receiving different treatments as indicated. Black arrows indicated the large bubbles of the plasma membrane (scale bar:50 μm). (**B**) Fluorescence images of changes in membrane potential of mitochondria stained by JC-1 after different treatments (scale bar:100 μm). (**C**) Flow-cytometry analyses using annexin V and PI staining were performed to test the type of cell death in different groups. (**D**) Release of LDH in supernatant. (**E**) The expression of GSDME-N and cleaved-caspase-3 were examined by Western blot. GAPDH was used as an internal control. (**F**) and (**G**) The quantified levels of GSDME-N and cleaved-caspase-3 were analyzed by ImageJ software. *P<0.05, **P<0.01, *** P<0.001.

cells with normal morphology and more cells with pyroptosis characteristic morphology, which was more obvious in SPDT O_2NBs group.

After preliminary verification from cell morphology, we detected the changes of mitochondrial membrane potential using JC-1 dye after different treatments, as several researches had shown that the induction of pyroptosis was related to mitochondrial damage. As shown in Figure 4B, a strong red fluorescence signal (JC-1 aggregates) and a weak green fluorescence signal (JC-1 monomers) were observed in the control group, which meant that the mitochondrial membrane potential was not decreased, indicating the mitochondria were not damaged. In the remaining groups, the transition from red fluorescence to green fluorescence in different degrees was obviously observed, implying that the mitochondrial membrane potential decreased at different levels. The strongest green fluorescence signal and the weakest red fluorescence signal were reflected in SPDT O_2NBs group.

Next, we validated the typical characteristics of cell membrane rupture during pyroptosis, including annexin V and PI double staining as well as LDH release. Since annexin V could stain damaged cell membrane and PI could stain nucleic acids after cell membrane rupture, the double positive of annexin V and PI staining was able to verify pyroptosis to some extent. As shown in the flow cytometry results of Figure 4C, the percentage of double positive of annexin V and PI staining varied among different treatment groups, and the lowest percentage in the control group and the highest percentage in SPDT O_2NBs group could be observed. After flow cytometry validation, we detected the release of cytosolic components in the supernatant, which illustrated the rupture of cell membrane during pyroptosis from another perspective. Considering that the integrity of the plasma membrane was disrupted, the release of LDH was detected to represent the release of cytosolic contents. As expected, the cells after different treatments showed different degrees of LDH release compared with the control group (Figure 4D). Consistent with the results of flow cytometry, the release of LDH was the least in control group and the most in SPDT O_2NBs group.

Then, we detected the expression of pyroptosis related proteins using Western blot. Since ROS could activate caspase to form the effector component cleaved-caspase, and it had been reported that pyroptosis of TNBC cells was mainly induced through the cleaved-caspase-3/GSDME-N pathway, we first detected the expression of cleaved-caspase-3. As shown in Figure 4E–G, the expression level of cleaved-caspase-3 increased after different treatments compared with control group, and SPDT O_2NBs group had the highest expression level. Considering that cleaved-caspase-3 could cleave GSDME to form the active ingredient GSDME-N, which bound to the cell membrane and formed pores on it to induce pyroptosis, we next examined the expression of GSDME-N. The results showed that the expression level trend of GSDME-N was consistent with that of cleaved-caspase-3, indicating that cleaved-caspase-3 could indeed cleave GSDME to induce pyroptosis (Figure 4E–G).

Differential Expression Analysis Based on RNA-Seq

After validating SPDT O_2NBs-mediated pyroptosis, we examined its in-depth mechanism by RNA-seq. From the volcano plot results, it could be found that there were 628 mRNA differentially expressed before and after treatment, of which 370 were up-regulated and 258 were down-regulated, while there were 80 lncRNA differentially expressed, of which 31 were up-regulated and 49 were down-regulated (Figure 5A and B). Table 1 and Table 2 respectively listed the top 10 mRNA and lncRNA with the most significant differences, where mRNA mainly included CSF, TNFAIP3, CXCL, and IL, while lncRNA mainly included HLA-A, LPP, and PSME1, etc. All differentially expressed mRNA and lncRNA could be found in Tables S1 and S2. The results of mRNA and lncRNA differential clustering analysis were presented in the form of heatmaps, where red represented high expression and green represented low expression (Figure 5C and D).

GO, KEGG, Reactome, and DO Enrichment Analysis

Based on the results of differentially expressed genes, we conducted various analyses to explore their functions. GO enrichment mainly analyzed gene function, and it could be found that there were significant differences in mRNA-based GO enrichment results, such as "response to reactive oxygen species", "positive regulation of cytokine production", and "cellular response to biotic stimulus" (Figure 6A, E and Table S3). Similarly, "cellular response to type I interferon" and "serotonin receptor signaling pathway" exhibited differences in GO enrichment based on lncRNA (Figure 6B, F and Table S4). Significant enrichment in KEGG could ascertain the principal biochemical metabolic pathways and signal transduction routes that the candidate target

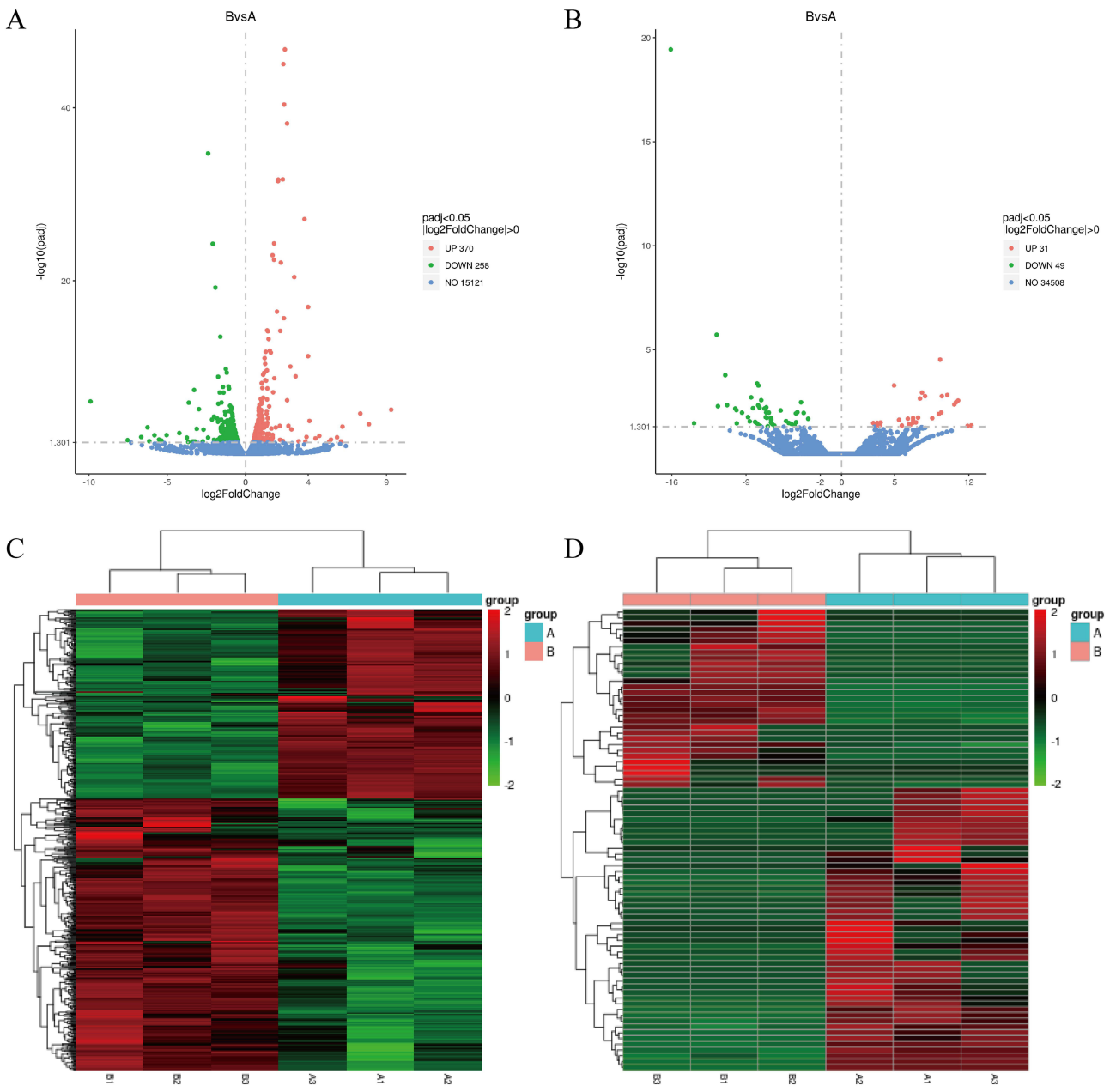

Figure 5 Differential expression analysis based on RNA-seq. (**A**) and (**B**) Volcano plot of differentially expressed mRNA and lncRNA transcripts. (**C**) and (**D**) Heat map of hierarchical clustering in the expression profiles of differentially expressed mRNA and lncRNA.

genes were engaged in. It could be observed that there was a difference in KEGG enrichment of mRNA between "HIF-1 signaling pathway", "TNF signaling pathway", and "IL-17 signaling pathway" (Figure 6C, G and Table S5). The KEGG enrichment of lncRNA could be observed in Figure 6D, H and Table S6. Reactome was a curated database of biological pathways that helped to elucidate the molecular mechanisms at play within biological systems. Reactome functional enrichment of mRNA revealed significant differences in "cellular senescence" and "interleukin signaling" (Figure 6I, 6M and Table S7), while "interferon alpha/beta signaling" and "VLDLR internalisation and degradation" were significantly different in lncRNA (Figure 6J, N and Table S8). DO was a database describing the relationship between gene function and disease. DO enrichment analysis of mRNA revealed that differentially expressed genes were associated with many cancers, such as breast cancer and pancreatic cancer (Figure 6K, O and Table S9). However, in the DO enrichment of lncRNA, although cancer species were screened, there was no statistical difference, which might be attributed to the number of samples (Figure 6L, P and Table S10).

Table 1 Top 10 mRNA with the Most Significant Differences

Gene_Name	Gene_Description	Log2FoldChange	pvalue	padj
CSF2	Colony stimulating factor 2	2.51273429	1.16E-51	1.79E-47
TNFAIP3	TNF alpha induced protein 3	2.415990696	8.51E-50	8.77E-46
CXCL1	C-X-C motif chemokine ligand 1	2.467935244	5.43E-45	4.20E-41
IL1A	Interleukin 1 alpha	2.656018208	1.09E-42	6.73E-39
ZC3H11A	Zinc finger CCCH-type containing 11A	−2.39365024	3.61E-39	1.86E-35
CXCL8	C-X-C motif chemokine ligand 8	2.378608846	4.33E-36	1.91E-32
CXCL2	C-X-C motif chemokine ligand 2	2.089517974	5.25E-36	2.03E-32
CSF3	Colony stimulating factor 3	2.076553225	8.84E-36	3.04E-32
CYP1A1	Cytochrome P450 family 1 subfamily A member 1	3.769705141	2.39E-31	7.40E-28
IL1B	Interleukin 1 beta	1.819645536	1.72E-28	4.84E-25

Notes: Log2FoldChange: multiples of differences between the two comparison groups. padj: the p value after correction.

Table 2 Top 10 lncRNA with the Most Significant Differences

Gene_Name	Gene_Description	Log2FoldChange	pvalue	padj
HLA-A	Major Histocompatibility complex, class I, A	−16.10905113	2.91E-25	3.67E-20
LPP	LIM domain containing preferred translocation partner in lipoma	−11.78060885	7.15E-10	1.92E-06
PSME1	Proteasome activator subunit 1	9.295635502	1.89E-08	2.98E-05
MALAT1	Metastasis associated lung adenocarcinoma transcript 1	−10.967943	1.46E-07	0.000168386
LINC01359	Long intergenic non-protein coding RNA 1359	−7.964675796	4.71E-07	0.000424375
KDM5B	Lysine demethylase 5B	4.950224519	6.06E-07	0.000530086
PIH1D1	PIH1 domain containing 1	−7.839343273	6.20E-07	0.000531961
DDX3X	DEAD-box helicase 3 X-linked	7.590418697	1.72E-06	0.001176332
KIAA1671	KIAA1671	9.977367786	2.38E-06	0.00151802
PLEKHH2	Pleckstrin homology, MyTH4 and FERM domain containing H2	9.463738503	2.87E-06	0.001724487

Notes: Log2FoldChange: multiples of differences between the two comparison groups. padj: the p value after correction.

Discussion

Even though considerable attempts have been dedicated to enhancing the outcomes for TNBC, the results are not to meet expectations. Consequently, the pursuit of innovative therapeutic approaches for TNBC holds significant value. In this study, the gas core of IR780-loaded NBs was filled with oxygen. After sequentially applying US and NIR irradiation, NBs rapidly ruptured and produced UTND effect, releasing oxygen and promoting IR780 to enter tumor cells. The released oxygen improved tumor hypoxia and the stimulated IR780 simultaneously exerted SDT and PDT effects, producing a large amount of ROS to kill tumors. Subsequently, we found that pyroptosis was the lethal mechanism induced by IR780@O_2 NBs. Finally, RNA-seq detected intrinsically differentially expressed genes and multiple enrichment analyses revealed potential signaling pathways.

SPDT integrates SDT and PDT, exhibiting a synergistic effect in killing tumor cells. US and NIR activate sonosensitizers and photosensitizers, generating SDT and PDT effects, which not only produce a large amount of ROS for anti-tumor action but also effectively eliminate deep-seated tumor tissues.[27] This study employed the dual-stimuli responsive material IR780 to achieve both SDT and PDT. Compared to the nanoplatforms that required the separate incorporation of sonosensitizers and photosensitizers for SPDT, our approach, which used a single material for dual purposes, was simpler to synthesize and had superior biocompatibility, increasing the potential for clinical translation. Moreover, studies have shown that IR780 has affinity for organic anion transport peptides, allowing it to selectively accumulate in the mitochondria of tumor cells without the need for tumor-targeting molecules.[28,29] Compared to some sono- or photosensitizers, IR780 poses a greater threat to tumor tissues because the mitochondria, being the metabolic hub of the cell, will lead to insufficient cellular energy supply when specifically damaged.[29,30]

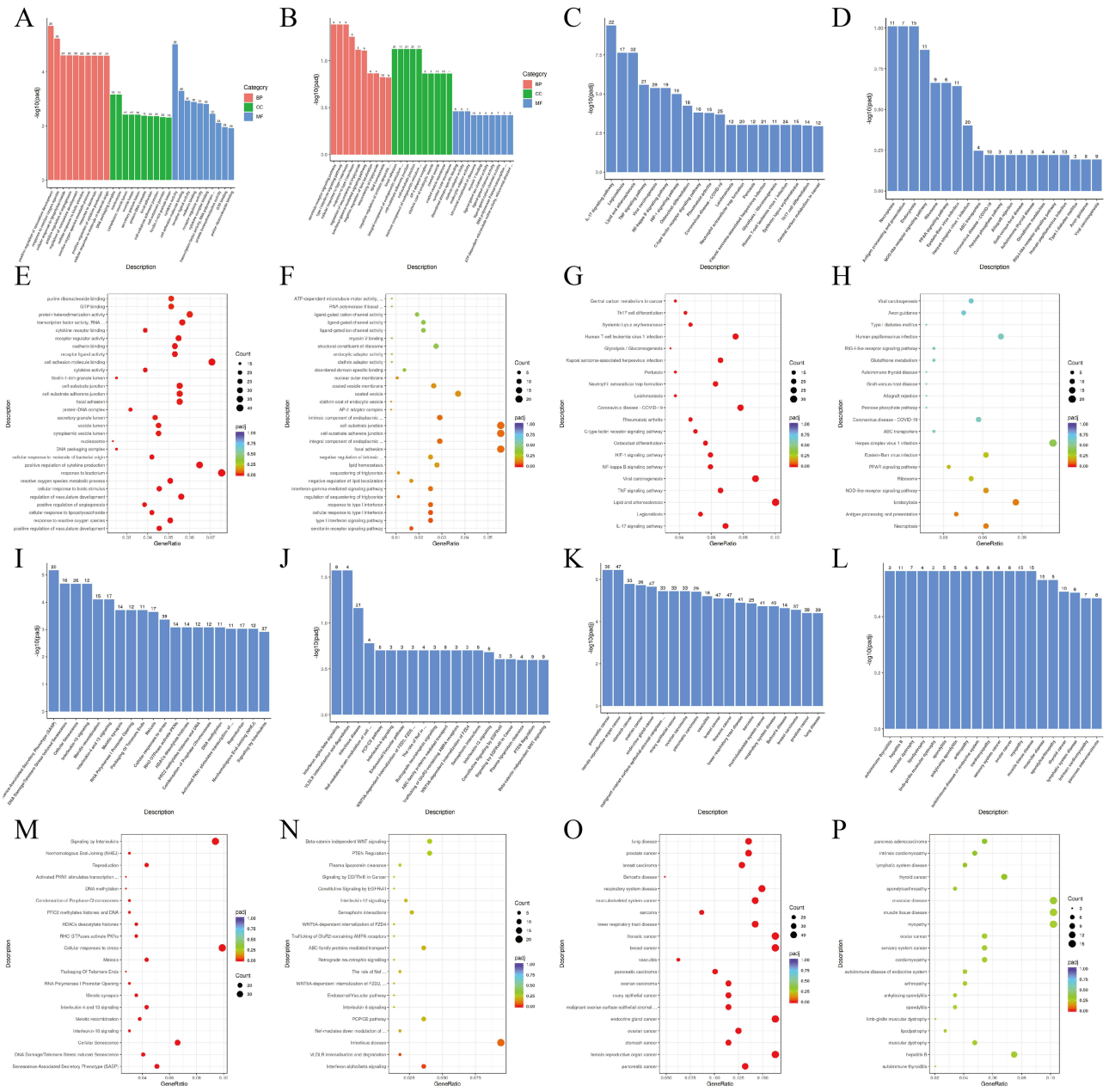

Figure 6 GO, KEGG, Reactome, and DO enrichment analysis. (**A**) and (**B**) The bar chart of GO pathways enriched with mRNA and lncRNA differentially expressed. (**C**) and (**D**) The bar chart of KEGG pathways enriched with mRNA and lncRNA differentially expressed. (**E**) and (**F**) The scatter plot of GO pathways enriched with mRNA and lncRNA differentially expressed. (**G**) and (**H**) The scatter plot of KEGG pathways enriched with mRNA and lncRNA differentially expressed. (**I**) and (**J**) The bar chart of Reactome pathways enriched with mRNA and lncRNA differentially expressed. (**K**) and (**L**) The bar chart of DO pathways enriched with mRNA and lncRNA differentially expressed. (**M**) and (**N**) The scatter plot of Reactome pathways enriched with mRNA and lncRNA differentially expressed. (**O**) and (**P**) The scatter plot of DO pathways enriched with mRNA and lncRNA differentially expressed.

NBs have many advantages, such as strong stability, high biocompatibility, and ease of modification, playing a significant role in drug delivery.[31,32] After US irradiation, NBs will contract and rupture abruptly, generating jets, shock waves, and high pressure, which are known as cavitation effect.[33] The mechanical and chemical energy produced by cavitation effect lead to the formation of reversible small pores in the cell membrane, increasing its permeability and fluidity.[33] The drugs released from the NBs can enter the tumor cells through these reversible small pores, leading to an increased local drug concentration within the cells, which significantly enhances the killing effect on tumor cells.[34] Although there are currently studies combining UTND and SDT, few studies combining with SPDT. In this study, the

synthesized IR780@O_2 NBs had a particle size distribution of 395 ± 2.94 nm, and no significant change in particle size was observed after 15 d of preparation, indicating good stability. The results of zeta potential and UV absorption confirmed that IR780 was successfully loaded onto the NBs. Experiments such as CCK-8, live/dead staining, and ROS detection verified that the NBs could enhance the SPDT therapeutic effect produced by IR780, which was attributed to the increased accumulation of IR780 within tumor cells through the UTND effect.

Despite the fact that NBs can enhance the therapeutic efficacy of IR780 through the UTND effect, the TME is typically hypoxic, which severely impairs the effectiveness of SPDT.[35] Hypoxia is a characteristic hallmark of malignant tumors.[35] On the one hand, due to metabolic upregulation, the proliferation and replication pace of cancer cells outstrip that of normal cells by several folds, resulting in a higher oxygen consumption.[36] On the other hand, neovascularization is a common strategy used by tumor tissues to deliver oxygen and nutrients, adapting to the hypoxic conditions. However, these newly formed blood vessels are typically immature, characterized by their elongation, dilation, and tortuosity.[37,38] The chaotic blood flow within the tumor and the compromised vascular network produces a gradient of oxygen tension and exacerbate local hypoxia.[37,38] Research indicates that hypoxia not only increases the malignancy of tumors and triggers the metastasis of tumor cells, but also enhances the resistance of tumor cells to chemotherapy, radiotherapy, ROS-dependent therapies, and immunotherapy.[39] Therefore, overcoming the limitations of the hypoxic TME during the treatment process through various methods is crucial for improving the therapeutic effect. Currently, some studies focus on using metal ions to catalyze the production of oxygen from H_2O_2 within tumor cells to alleviate hypoxia.[39–41] However, the limited content of H_2O_2 in the TME restricts the production of oxygen. Other studies involve the delivery of oxygen through hemoglobin-based preparations, but their oxygen-carrying capacity needs to be further improved.[42] Although the oxygen-carrying efficiency of perfluorocarbons is inherently higher than that of hemoglobin-based preparations, they are unstable and prone to spontaneously convert into gas, leading to significant losses during the preparation process.[43] In comparison, this study utilized NBs to carry oxygen to ameliorate the hypoxic TME. Unlike metal ion catalysis, it was not limited by the insufficient presence of the reactant H_2O_2 in the TME. Moreover, NBs naturally carried a gas core, which simplified the production steps and made synthesis more straightforward. Additionally, the particle size distribution at 0 d and 15 d indicated that the prepared oxygen-enriched NBs had good stability. The ROS detection results showed that the oxygen-enriched NBs produced more ROS than the regular NBs, proving that the oxygen carried by the NBs was successfully utilized by the SPDT. Other experimental results also demonstrated that the oxygen-enriched NBs had better therapeutic effects compared to the regular NBs.

In recent years, there has been a surge in research on pyroptosis, which is recognized as a novel type of programmed cell death. Researchers have shown that various chemotherapeutic drugs, such as cisplatin, paclitaxel, and doxorubicin, can activate caspase-3/GSDME through the production of ROS, inducing pyroptosis in TNBC cells.[23] Li et al found that PDT could induce esophageal cancer cells to undergo pyroptosis through the caspase-3/GSDME pathway, and Chen et al confirmed that SDT induced pyroptosis in TNBC cells via the caspase-3/GSDME pathway.[44,45] Additionally, the latest research has found that during pyroptosis, the damage to the cell membrane releases a variety of intracellular contents, including tumor-associated antigens, LDH and inflammatory cytokines.[46] At the same time, the occurrence of pyroptosis also accelerates the release of damage-associated molecular patterns (DAMPs), inducing immunogenic cell death (ICD), thereby triggering a strong and sustained anti-tumor immune response.[46] Therefore, it is necessary to explore an effective way to induce pyroptosis in tumor cells. This study utilized the dual-stimuli responsiveness of IR780 to generate a large amount of ROS that killed TNBC cells. Cellular morphology monitoring, JC-1 assays, LDH release, Annexin V/PI double staining, and Western blotting validated that the SPDT induced TNBC cell death through the pyroptosis pathway. Furthermore, oxygen enriched NBs were able to increase the accumulation of IR780 in tumor cells and improve the hypoxic TME, enhancing the extent of pyroptosis induced by SPDT.

RNA-seq, as a tool for uncovering molecular mechanisms, has been widely utilized.[47,48] Similarly, after demonstrating that IR780@O_2 NBs-induced TNBC cell death through the pyroptosis pathway, we performed RNA-seq analysis on the cells before and after treatment, with the aim of revealing the intrinsic mechanisms by which this method induced pyroptosis. Among the most significant differentially expressed genes, some were widely demonstrated to be associated with pyroptosis, such as TNF and IL, while there were few reports linking CSF and CXCL to pyroptosis, suggesting they might be potential targets for inducing pyroptosis.[21,49] In various enrichment analyses, "response to reactive oxygen species" and "HIF-1 signaling pathway" exhibited significant differences, which from one aspect demonstrated that the

methods employed in this study could induce pyroptosis in TNBC through ROS and also alleviate tumor hypoxia. Additionally, the changes in "TNF signaling pathway", "interferon alpha/beta signaling", and "interleukin signaling" indicated that the methods used in this study had the potential to induce tumor immune responses, which was consistent with the occurrence of pyroptosis.[19,50] It was noteworthy that cell senescence played an important role in the development of tumors, and there was significant difference between before and after treatment in this study, suggesting a potential link between senescence and pyroptosis, which had rarely been reported in previous studies.[51,52]

Although this study successfully prepared IR780@O_2 NBs and verified their ability to induce pyroptosis in TNBC cells, there were still some shortcomings. The particle size of IR780@O_2 NBs utilized in this study was slightly larger than that of conventional nanoparticles, which might affect the application in vivo, and it should be further optimized to reduce particle size in the future. According to the literature reports, TNBC mainly underwent pyroptosis through non classical pathways. This study only verified the expression of caspase-3/GSDME, and did not detect the expression of caspase-1/GSDMD related proteins, lacking a certain degree of rigor. Subsequent experiments needed to improve the detection of classical pathway protein to verify whether caspase-1/GSDMD related proteins played a role in TNBC cell pyroptosis. In addition, this study only validated one type of TNBC cell line and conducted in vitro cell experiments. Further testing of multiple TNBC cell lines was needed, and in vivo experiments needed to be improved to make the experimental results more convincing.

Conclusions

In this study, IR780@O_2 NBs, which possessed photoacoustic dual response characteristics as well as the capability to ameliorate hypoxia, was successfully synthesized. Additionally, it was confirmed that IR780@O_2 NBs- mediated SPDT could induce the death of TNBC cells through the pyroptosis pathway. The in-depth mechanism revealed that CSF and CXCL could be potential targets for the occurrence of pyroptosis in TNBC cells, and cellular senescence might be a biological process closely related to pyroptosis. In general, this study explored a new nanoplatform to improve hypoxia and enhance pyroptosis, and revealed potential targets of pyroptosis in TNBC, which might provide certain value for future research.

Funding

This research was supported by the National Natural Science Foundation of China (grant number 82171953) and the Fundamental Research Funds for the Provincial Universities (grant number 2021-KYYWF-0251).

Disclosure

The authors declare that there are no conflicts of interest regarding this study.

References

1. Kwapisz D. Pembrolizumab and atezolizumab in triple-negative breast cancer. *Cancer Immunol Immunother*. 2021;70(3):607–617. doi:10.1007/s00262-020-02736-z
2. Leon-Ferre RA, Goetz MP. Advances in systemic therapies for triple negative breast cancer. *BMJ*. 2023;381:e071674. doi:10.1136/bmj-2022-071674
3. He X, Zhang S, Tian Y, Cheng W, Jing H. Research Progress of Nanomedicine-Based Mild Photothermal Therapy in Tumor. *Int J Nanomed*. 2023;18:1433–1468. doi:10.2147/IJN.S405020
4. Chow JCL. Application of Nanomaterials in Biomedical Imaging and Cancer Therapy II. *Nanomaterials*. 2024;14(20):1627. doi:10.3390/nano14201627
5. Siddique S, Chow JCL. Gold Nanoparticles for Drug Delivery and Cancer Therapy. *Appl Sci*. 2020;10(11):3824. doi:10.3390/app10113824
6. Liu X, Lu Y, Li X, Luo L, You J. Nanoplatform-enhanced photodynamic therapy for the induction of immunogenic cell death. *J Control Release*. 2024;365:1058–1073. doi:10.1016/j.jconrel.2023.11.058
7. Jiang L, Liu L, Lv F, Wang S, Ren X. Integration of Self-Luminescence and Oxygen Self-Supply: a Potential Photodynamic Therapy Strategy for Deep Tumor Treatment. *Chempluschem*. 2020;85(3):510–518. doi:10.1002/cplu.202000083
8. Li J, Yue Z, Tang M, et al. Strategies to Reverse Hypoxic Tumor Microenvironment for Enhanced Sonodynamic Therapy. *Adv Healthc Mater*. 2024;13(1):e2302028. doi:10.1002/adhm.202302028
9. Li D, Zhang Z. TRIM37 promotes the aggressiveness of ovarian cancer cells and increases c-Myc expression by binding to HUWE1. *Arch Biochem Biophys*. 2022;728:109372. doi:10.1016/j.abb.2022.109372

10. Wang L, Li G, Cao L, et al. An ultrasound-driven immune-boosting molecular machine for systemic tumor suppression. *Sci Adv*. 2021;7(43): eabj4796. doi:10.1126/sciadv.abj4796
11. Liu L, Zhang J, An R, et al. Smart Nanosensitizers for Activatable Sono-Photodynamic Immunotherapy of Tumors by Redox-Controlled Disassembly. *Angew Chem Int Ed Engl*. 2023;62(10):e202217055. doi:10.1002/anie.202217055
12. Nene LC, Abrahamse H. Design consideration of phthalocyanines as sensitizers for enhanced sono-photodynamic combinatorial therapy of cancer. *Acta Pharm Sin B*. 2024;14(3):1077–1097. doi:10.1016/j.apsb.2023.11.030
13. Wysocki M, Czarczynska-Goslinska B, Ziental D, Michalak M, Güzel E, Sobotta L. Excited State and Reactive Oxygen Species against Cancer and Pathogens: a Review on Sonodynamic and Sono-Photodynamic Therapy. *ChemMedChem*. 2022;17(13):e202200185. doi:10.1002/cmdc.202200185
14. Nomikou N, Sterrett C, Arthur C, McCaughan B, Callan JF, McHale AP. The effects of ultrasound and light on indocyanine-green-treated tumour cells and tissues. *ChemMedChem*. 2012;7(8):1465–1471. doi:10.1002/cmdc.201200233
15. Zhu J, Wang Y, Yang P, et al. GPC3-targeted and curcumin-loaded phospholipid microbubbles for sono-photodynamic therapy in liver cancer cells. *Colloids Surf B*. 2021;197:111358. doi:10.1016/j.colsurfb.2020.111358
16. Zheng X, Sun W, Ju M, Wu J, Huang H, Shen B. A chemical biology toolbox to overcome the hypoxic tumor microenvironment for photodynamic therapy: a review. *Biomater Sci*. 2022;10(17):4681–4693. doi:10.1039/D2BM00776B
17. Tang W, Han L, Lu X, et al. A Nucleic Acid/Gold Nanorod-Based Nanoplatform for Targeted Gene Editing and Combined Tumor Therapy. *ACS Appl Mater Interfaces*. 2021;13(18):20974–20981. doi:10.1021/acsami.1c02122
18. Chen Y, Shang H, Wang C, et al. RNA-Seq Explores the Mechanism of Oxygen-Boosted Sonodynamic Therapy Based on All-in-One Nanobubbles to Enhance Ferroptosis for the Treatment of HCC. *Int J Nanomed*. 2022;17:105–123. doi:10.2147/IJN.S343361
19. Rao Z, Zhu Y, Yang P, et al. Pyroptosis in inflammatory diseases and cancer. *Theranostics*. 2022;12(9):4310–4329. doi:10.7150/thno.71086
20. Yu P, Zhang X, Liu N, Tang L, Peng C, Chen X. Pyroptosis: mechanisms and diseases. *Signal Transduct Target Ther*. 2021;6(1):128. doi:10.1038/s41392-021-00507-5
21. Fang Y, Tian S, Pan Y, et al. Pyroptosis: a new frontier in cancer. *Biomed Pharmacother*. 2020;121:109595. doi:10.1016/j.biopha.2019.109595
22. An H, Heo JS, Kim P, et al. Tetraarsenic hexoxide enhances generation of mitochondrial ROS to promote pyroptosis by inducing the activation of caspase-3/GSDME in triple-negative breast cancer cells. *Cell Death Dis*. 2021;12(2):159. doi:10.1038/s41419-021-03454-9
23. Zhang Z, Zhang H, Li D, Zhou X, Qin Q, Zhang Q. Caspase-3-mediated GSDME induced Pyroptosis in breast cancer cells through the ROS/JNK signalling pathway. *J Cell Mol Med*. 2021;25(17):8159–8168. doi:10.1111/jcmm.16574
24. Smail C, Montgomery SB. RNA Sequencing in Disease Diagnosis. *Annu Rev Genomics Hum Genet*. 2024;25(1):353–367. doi:10.1146/annurev-genom-021623-121812
25. Xu Z, Wang Y, Sheng K, et al. Droplet-based high-throughput single microbe RNA sequencing by smRandom-seq. *Nat Commun*. 2023;14(1):5130. doi:10.1038/s41467-023-40137-9
26. Vasconcelos CFM, Ribas VT, Petrs-Silva H. Shared Molecular Pathways in Glaucoma and Other Neurodegenerative Diseases: insights from RNA-Seq Analysis and miRNA Regulation for Promising Therapeutic Avenues. *Cells*. 2023;12(17):2155. doi:10.3390/cells12172155
27. Liao S, Cai M, Zhu R, et al. Antitumor Effect of Photodynamic Therapy/Sonodynamic Therapy/Sono-Photodynamic Therapy of Chlorin e6 and Other Applications. *Mol Pharm*. 2023;20(2):875–885. doi:10.1021/acs.molpharmaceut.2c00824
28. Bao J, Zhao Y, Xu J, Guo Y. Design and construction of IR780- and EGCG-based and mitochondrial targeting nanoparticles and their application in tumor chemo-phototherapy. *J Mater Chem B*. 2021;9(48):9932–9945. doi:10.1039/D1TB01899J
29. Gan H, Huang X, Luo X, et al. A Mitochondria-Targeted Ferroptosis Inducer Activated by Glutathione-Responsive Imaging and Depletion for Triple Negative Breast Cancer Theranostics. *Adv Healthc Mater*. 2023;12(22):e2300220. doi:10.1002/adhm.202300220
30. Zhang T, Wu B, Akakuru OU, et al. Hsp90 inhibitor-loaded IR780 micelles for mitochondria-targeted mild-temperature photothermal therapy in xenograft models of human breast cancer. *Cancer Lett*. 2021;500:41–50. doi:10.1016/j.canlet.2020.12.028
31. Ma Y, Li J, Zhao Y, Hu B, Liu Y, Liu C. Nanobubble-mediated co-delivery of Ce6 and miR-195 for synergized sonodynamic and checkpoint blockade combination therapy with elicitation of robust immune response in hepatocellular carcinoma. *Eur J Pharm Biopharm*. 2022;181:36–48. doi:10.1016/j.ejpb.2022.10.017
32. Li H, Zhang Y, Shu H, Lv W, Su C, Nie F. Highlights in ultrasound-targeted microbubble destruction-mediated gene/drug delivery strategy for treatment of malignancies. *Int J Pharm*. 2022;613:121412. doi:10.1016/j.ijpharm.2021.121412
33. Lentacker I, De Cock I, Deckers R, De Smedt SC, Moonen CTW. Understanding ultrasound induced sonoporation: definitions and underlying mechanisms. *Adv Drug Deliv Rev*. 2014;72:49–64. doi:10.1016/j.addr.2013.11.008
34. Jing Y, Xiu-Juan Z, Hong-Jiao C, et al. Ultrasound-targeted microbubble destruction improved the antiangiogenic effect of Endostar in triple-negative breast carcinoma xenografts. *J Cancer Res Clin Oncol*. 2019;145(5):1191–1200. doi:10.1007/s00432-019-02866-7
35. Liu H, Jiang W, Wang Q, Hang L, Wang Y, Wang Y. ROS-sensitive biomimetic nanocarriers modulate tumor hypoxia for synergistic photodynamic chemotherapy. *Biomater Sci*. 2019;7(9):3706–3716. doi:10.1039/C9BM00634F
36. Xu -X-X, Chen S-Y, Yi N-B, et al. Research progress on tumor hypoxia-associative nanomedicine. *J Control Release*. 2022;350:829–840. doi:10.1016/j.jconrel.2022.09.003
37. Liang Q, Zhou L, Li Y, Liu J, Liu Y. Nano drug delivery system reconstruct tumour vasculature for the tumour vascular normalisation. *J Drug Target*. 2022;30(2):119–130. doi:10.1080/1061186X.2021.1927056
38. Li Z, Ning F, Wang C, Yu H, Ma Q, Sun Y. Normalization of the tumor microvasculature based on targeting and modulation of the tumor microenvironment. *Nanoscale*. 2021;13(41):17254–17271. doi:10.1039/D1NR03387E
39. He M, Chen Y, Tao C, et al. Mn-Porphyrin-Based Metal-Organic Framework with High Longitudinal Relaxivity for Magnetic Resonance Imaging Guidance and Oxygen Self-Supplementing Photodynamic Therapy. *ACS Appl Mater Interfaces*. 2019;11(45):41946–41956. doi:10.1021/acsami.9b15083
40. Zhang X, Min Y, Zhang Q, et al. Functionalized Mn3 O4 Nanosheets with Photothermal, Photodynamic, and Oxidase-Like Activities Triggered by Low-Powered Near-Infrared Light for Synergetic Combating Multidrug-Resistant Bacterial Infections. *Adv Healthc Mater*. 2022;11(12):e2200121. doi:10.1002/adhm.202200121
41. Liu J, Du P, Liu T, et al. A black phosphorus/manganese dioxide nanoplatform: oxygen self-supply monitoring, photodynamic therapy enhancement and feedback. *Biomaterials*. 2019;192:179–188. doi:10.1016/j.biomaterials.2018.10.018

42. Luo Z, Zheng M, Zhao P, et al. Self-Monitoring Artificial Red Cells with Sufficient Oxygen Supply for Enhanced Photodynamic Therapy. *Sci Rep*. 2016;6(1):23393. doi:10.1038/srep23393
43. Hong L, Pliss AM, Zhan Y, et al. Perfluoropolyether Nanoemulsion Encapsulating Chlorin e6 for Sonodynamic and Photodynamic Therapy of Hypoxic Tumor. *Nanomaterials*. 2020;10(10):2058. doi:10.3390/nano10102058
44. Li L, Song D, Qi L, et al. Photodynamic therapy induces human esophageal carcinoma cell pyroptosis by targeting the PKM2/caspase-8/caspase-3/GSDME axis. *Cancer Lett*. 2021;520:143–159. doi:10.1016/j.canlet.2021.07.014
45. Chen Z, Liu W, Yang Z, et al. Sonodynamic-immunomodulatory nanostimulators activate pyroptosis and remodel tumor microenvironment for enhanced tumor immunotherapy. *Theranostics*. 2023;13(5):1571–1583. doi:10.7150/thno.79945
46. Tang Y, Bisoyi HK, Chen X-M, et al. Pyroptosis-Mediated Synergistic Photodynamic and Photothermal Immunotherapy Enabled by a Tumor-Membrane-Targeted Photosensitive Dimer. *Adv Mater*. 2023;35(25):e2300232. doi:10.1002/adma.202300232
47. McDermaid A, Monier B, Zhao J, Liu B, Ma Q. Interpretation of differential gene expression results of RNA-seq data: review and integration. *Brief Bioinform*. 2019;20(6):2044–2054. doi:10.1093/bib/bby067
48. Saeidian AH, Youssefian L, Vahidnezhad H, Uitto J. Research Techniques Made Simple: whole-Transcriptome Sequencing by RNA-Seq for Diagnosis of Monogenic Disorders. *J Invest Dermatol*. 2020;140(6):1117–1126.e1. doi:10.1016/j.jid.2020.02.032
49. Wang Y, Zhang H, Chen Q, et al. TNF-α/HMGB1 inflammation signalling pathway regulates pyroptosis during liver failure and acute kidney injury. *Cell Prolif*. 2020;53(6):e12829. doi:10.1111/cpr.12829
50. Hsu S-K, Li C-Y, Lin IL, et al. Inflammation-related pyroptosis, a novel programmed cell death pathway, and its crosstalk with immune therapy in cancer treatment. *Theranostics*. 2021;11(18):8813–8835. doi:10.7150/thno.62521
51. Jha SK, De Rubis G, Devkota SR, et al. Cellular senescence in lung cancer: molecular mechanisms and therapeutic interventions. *Ageing Res Rev*. 2024;97:102315. doi:10.1016/j.arr.2024.102315
52. Wang X, Fukumoto T, Noma K-I. Therapeutic strategies targeting cellular senescence for cancer and other diseases. *J Biochem*. 2024;175(5):525–537. doi:10.1093/jb/mvae015